Cross section for $\gamma n \rightarrow \pi^0 n$ measured at the Mainz A2 experiment

W. J. Briscoe,[1] M. Hadžimehmedović,[2] A. E. Kudryavtsev,[3,1] V. V. Kulikov,[3] M. A. Martemianov,[3] I. I. Strakovsky ⬤,[1,*]
A. Švarc,[4,5] V. E. Tarasov,[3] R. L. Workman,[1] S. Abt,[6] P. Achenbach,[7] C. S. Akondi,[8] F. Afzal,[9] P. Aguar-Bartolomé,[7]
Z. Ahmed,[10] J. R. M. Annand,[11] H. J. Arends,[7] K. Bantawa,[8] M. Bashkanov,[12] R. Beck,[9] M. Biroth,[7] N. Borisov,[13]
A. Braghieri,[14] S. A. Bulychjov,[3] F. Cividini,[7] C. Collicott,[15] S. Costanza,[16,14] A. Denig,[7] E. J. Downie,[1] P. Drexler,[7] S. Fegan,[1]
M. I. Ferretti Bondy,[7] S. Gardner,[11] D. Ghosal,[6] D. I. Glazier,[11] I. Gorodnov,[13] W. Gradl,[7] M. Günther,[6] D. Gurevich,[17]
L. Heijkenskjöld,[7] D. Hornidge,[18] G. M. Huber,[10] A. Käser,[6] V. L. Kashevarov,[7,13] S. Kay,[10] M. Korolija,[4,5] B. Krusche,[6]
A. Lazarev,[13] K. Livingston,[11] S. Lutterer,[6] I. J. D. MacGregor,[11] R. Macrae,[11] D. M. Manley,[8] P. P. Martel,[7] J. C. McGeorge,[11]
D. G. Middleton,[7,18] R. Miskimen,[19] E. Mornacchi,[7] A. Mushkarenkov,[14,19] C. Mullen,[11] A. Neganov,[13] A. Neiser,[7]
M. Ostrick,[7] P. B. Otte,[7] H. Osmanović,[2] R. Omerović,[2] B. Oussena,[7,1] D. Paudyal,[10] P. Pedroni,[14] A. Powell,[11]
S. N. Prakhov,[7,20] G. Ron,[21,1] T. Rostomyan,[6] A. Sarty,[15] C. Sfienti,[7] V. Sokhoyan,[7] K. Spieker,[9] J. Stahov,[2] O. Steffen,[7]
I. Supek,[4,5] A. Thiel,[9,11] M. Thiel,[7] A. Thomas,[7] L. Tiator,[7] M. Unverzagt,[7] Yu. A. Usov,[13] N. K. Walford,[6] D. P. Watts,[12]
S. Wagner,[7] D. Werthmüller,[12] J. Wettig,[7] M. Wolfes,[7] and N. Zachariou[12]

(A2 Collaboration at MAMI)

[1]*Institute for Nuclear Studies, Department of Physics, The George Washington University, Washington, DC 20052, USA*
[2]*University of Tuzla, Faculty of Natural Sciences and Mathematics, Univerzitetska 4, 75000 Tuzla, Bosnia and Herzegovina*
[3]*National Research Centre "Kurchatov Institute", Institute for Theoretical and Experimental Physics (ITEP), Moscow 117218, Russia*
[4]*Rudjer Bošković Institute, Bijenička cesta 54, 10002 Zagreb, Croatia*
[5]*Tesla Biotech, Mandlova 7, 10002 Zagreb, Croatia*
[6]*Department of Physics, University of Basel, Ch-4056 Basel, Switzerland*
[7]*Institut für Kernphysik, University of Mainz, D-55099 Mainz, Germany*
[8]*Kent State University, Kent, Ohio 44242, USA*
[9]*Helmholtz-Institut für Strahlen- und Kernphysik, University Bonn, D-53115 Bonn, Germany*
[10]*University of Regina, Regina, SK S4S-0A2 Canada*
[11]*SUPA School of Physics and Astronomy, University of Glasgow, Glasgow, G12 8QQ, United Kingdom*
[12]*Department of Physics, University of York, Heslington, York, Y010 5DD, United Kingdom*
[13]*Joint Institute for Nuclear Research, RU-141980 Dubna, Russia*
[14]*INFN Sezione di Pavia, I-27100 Pavia, Pavia, Italy*
[15]*Department of Astronomy and Physics, Saint Mary's University, E4L1E6 Halifax, Canada*
[16]*Dipartimento di Fisica, Università di Pavia, I-27100 Pavia, Italy*
[17]*Institute for Nuclear Research, RU-125047 Moscow, Russia*
[18]*Mount Allison University, Sackville, New Brunswick E4L1E6, Canada*
[19]*University of Massachusetts, Amherst, Massachusetts 01003, USA*
[20]*University of California Los Angeles, Los Angeles, California 90095, USA*
[21]*Racah Institute of Physics, Hebrew University of Jerusalem, Jerusalem 91904, Israel*

The $\gamma n \rightarrow \pi^0 n$ differential cross section evaluated for 27 energy bins span the photon-energy range 290–813 MeV ($W = 1.195$–1.553 GeV) and the pion c.m. polar production angles, ranging from $18°$ to $162°$, making use of model-dependent nuclear corrections to extract π^0 production data on the neutron from measurements on the deuteron target. Additionally, the total photoabsorption cross section was measured. The tagged photon beam produced by the 883 MeV electron beam of the Mainz Microtron MAMI was used for the π^0-meson production. Our accumulation of 3.6×10^6 $\gamma n \rightarrow \pi^0 n$ events allowed a detailed study of the reaction dynamics. Our data are in reasonable agreement with previous A2 measurements and extend them to lower energies. The data are compared with predictions of previous SAID, MAID, and BnGa partial-wave analyses and to the latest SAID fit MA19 that included our data. Selected photon-decay amplitudes $N^* \rightarrow \gamma n$ at the resonance poles are determined for the first time.

---

*igor@gwu.edu

I. INTRODUCTION

The N^* and Δ^* families of nucleon resonances have many well-established members [1], several of which overlap, having very similar masses and widths but different J^P spin-parity values. There are two closely spaced states above the famous $\Delta(1232)3/2^+$ resonance: $N(1520)3/2^-$ and $N(1535)1/2^-$.

One critical issue in the study of meson photoproduction on the nucleon comes from isospin. While isospin can change at the photon vertex, it must be conserved at the final hadronic vertex. The isospin amplitudes for the $\gamma N \to \pi N$ reactions are decomposed into three distinct $I = 1/2$ (proton and neutron) and $I = 3/2$ isospin components, $A_{\gamma, \pi^0 p/n} = \pm A_{p/n}^{I=1/2} + \frac{2}{3}A^{I=3/2}$ and $A_{\gamma, \pi^\pm} = \sqrt{2}(A_{p/n}^{I=1/2} \mp \frac{1}{3}A^{I=3/2})$ (see Ref. [2]). This expression indicates that the $I = 3/2$ multipoles can be entirely determined from proton target data. However, measurements from datasets with both neutron and proton targets are required to determine the isospin $I = 1/2$ amplitudes and to separate the $\gamma p N^*$ and $\gamma n N^*$ photon couplings. Only with good data on both proton and neutron targets can one hope to disentangle the isoscalar and isovector electromagnetic (EM) couplings of the various N^* and Δ^* resonances [3,4], as well as the isospin properties of the nonresonant background amplitudes. The lack of $\gamma n \to \pi^- p$ and $\gamma n \to \pi^0 n$ data [5] does not allow us to be as confident about the determination of neutron couplings compared with those of the proton. Some of the N^* baryons [$N(1520)3/2^-$, for instance] have stronger EM couplings to the neutron relative to the proton, while others [for instance, the nearby $N(1535)1/2^-$] have weaker EM couplings to the neutron relative to the proton. However, the resonance parameters of both these states are very uncertain, see Table I.

In the SAID πN partial-wave analysis (PWA), one can determine πN amplitudes by fitting the πN elastic data (up to $W = 2.5$ GeV) [6,7]. Resonances are then found through a search for poles in the complex energy plane. The SAID group considers mainly poles which are not far away from the physical axis. It is important to emphasize that these resonances are not put in by hand, contrary to the Breit-Wigner (BW) parametrization. The poles arise, in a sense, dynamically as a result of the enforced (quasi-) two-body unitarity cuts and the fit to the observable on the real energy axis. The photoproduction multipoles can be parametrized by using a form containing the Born terms (with no free parameters), phenomenological pieces maintaining the correct threshold behavior, and Migdal-Watson's theorem [8,9] below the two-pion production threshold. The πN matrix connects each multipole to structure found in the elastic-scattering analysis. The parametrization above the two-pion production threshold is based on a unitary K-matrix approach, with no strong constraints on the energy dependence apart from correct threshold properties.

Knowledge of the N^* and Δ^* resonance decay amplitudes into nucleons and photons is largely restricted to charged states. Apart from the lower-energy inverse reaction $\pi^- p \to \gamma n$ measurements, the extraction of the two-body $\gamma n \to \pi^- p$ and $\gamma n \to \pi^0 n$ observables requires the use of a model-dependent nuclear correction, which mainly comes from final-state interaction (FSI) effects within the deuteron. Most γn data are unpolarized and cover fairly narrow energy ranges. Of these, only about 1200 $\pi^0 n$ measurement data points exist, spanning the limited nucleon resonance region [5].

A FSI correction factor was defined as the ratio between a sum of leading diagrams and an impulse-approximation (IA) that the GWU-ITEP group then applied to the experimental γd data to get a two-body cross section for $\gamma n \to \pi^- p$ [10] and $\gamma n \to \pi^0 n$ [11]. The GWU SAID phenomenological amplitudes for πN and NN elastic scattering and $\gamma N \to \pi N$ were used as inputs to calculate the leading diagrams for the GWU-ITEP FSI code. The full Bonn potential was used for the deuteron description. Recently, the GWU-ITEP group determined $\gamma n \to \pi^- p$ differential cross sections from $\gamma d \to \pi^- pp$ measurements made by the CLAS [12,13] and MAMI/A2 [14] Collaborations. In this way, we succeeded in the first determination of neutron couplings at the pole positions for a number of baryons, such as $N(1440)1/2^+$, $N(1535)1/2^-$, $N(1650)1/2^-$, and $N(1720)3/2^+$, significantly improving the world data [13].

The $\gamma n \to \pi^0 n$ measurement on the deuteron target is much more complicated than $\gamma n \to \pi^- p$ because the π^0 can come from both γn and γp initial states. The GWU-ITEP studies have shown that photoproduction cross sections off the protons and neutrons are generally not equal [11]:

$$A(\gamma p \to \pi^0 p) = A_v + A_s, \quad A(\gamma n \to \pi^0 n) = A_v - A_s, \quad (1)$$

where A_v and A_s are isovector and isoscalar amplitudes, respectively, and $A_s \neq 0$. However, in the special case, in the region of the $\Delta(1232)3/2^+$ and $A_s = 0$, the FSI corrections for $\gamma p \to \pi^0 p$ and $\gamma n \to \pi^0 n$ cross sections are equal due to the isospin structure of the $\gamma N \to \pi N$ amplitudes.

Recently, the A2 Collaboration at MAMI published high-quality unpolarized and polarized measurements for π^0 photoproduction on a proton target below $W = 2$ GeV [15–20] while one study was carried out for π^0 photoproduction on the neutron [21,22] (the preliminary data were published in

TABLE I. Breit-Wigner (BW) mass and full width (in MeV) with proton $A_{3/2}(p)$ and $A_{1/2}(p)$, and with neutron $A_{3/2}(n)$ and $A_{1/2}(n)$ BW photon-decay amplitudes [in $(\text{GeV})^{-1/2} \times 10^{-3}$] from the PDG2018 [1] covering the energy range of the A2 experiment.

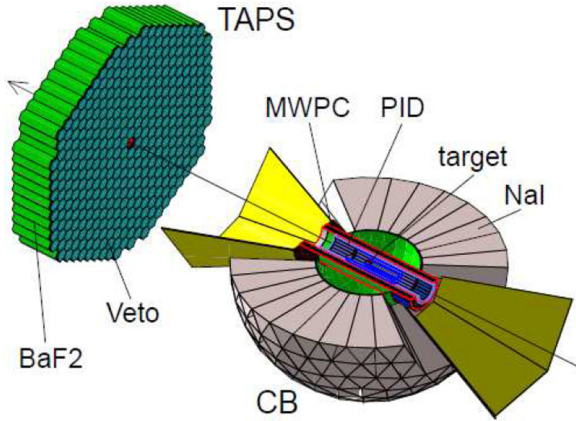| Resonance	M	Γ	$A_{3/2}(p)$	$A_{1/2}(p)$	$A_{3/2}(n)$	$A_{1/2}(n)$
$\Delta(1232)3/2^+$	1232 ± 2	117 ± 3	-255 ± 7	-135 ± 6		
$N(1440)1/2^+$	1440 ± 30	350 ± 100		-65 ± 15		$+45 \pm 10$
$N(1520)3/2^-$	1515 ± 15	110 ± 10	$+140 \pm 5$	-25 ± 8	-115 ± 8	-50 ± 8
$N(1535)1/2^-$	1530 ± 15	150 ± 25		$+105 \pm 15$		-75 ± 20

FIG. 1. Set-up of the A2 experiment. CB is a NaI(Tl) calorimeter, TAPS is a BaF$_2$ calorimeter which was not used for the present measurement, PID is a plastic scintillator detector for particle identification, MWPC are two cylindrical multiwire proportional chambers, target is a liquid deuterium target (see text for details).

Ref. [23]). This last study focuses on neutral pion photoproduction off the neutron using a deuteron target.

In the present paper, we report new, precise, $\gamma n \to \pi^0 n$ differential cross sections for $E = 290$ to 813 MeV in laboratory photon energy, corresponding to center-of-mass (c.m.) energy range from $W = 1.195$ to 1.553 GeV. Pion c.m. polar production angles, ranging from $\theta = 18°$ to $162°$, have been measured by the A2 Collaboration at MAMI. These new cross-section data have increased the world $\gamma n \to \pi^0 n$ database below $E = 2.7$ GeV by a significant amount [5]. Meanwhile, Ref. [22] covers $E = 446$–1427 MeV and $\theta = 32°$–$162°$.

The organization of this paper is as follows: In Sec. II, details of the A2 experiment and the A2 detector are given. Section III outlines the event selection and Sec. IV reviews the approach for determining the final-state interaction corrections. Section V presents and discusses the measured differential cross sections for the reaction $\gamma n \to \pi^0 n$. Section VI and L + P fit of the multipoles with determination of pole positions and residues. Finally, Sec. VII provides a summary of this work and the conclusions.

II. EXPERIMENTAL SETUP

The process $\gamma d \to \pi^0 np$ was measured by using the Crystal Ball (CB) [24] as the central spectrometer (Fig. 1). Our study shows that there is a marginal contribution from TAPS for the reaction $\gamma n \to \pi^0 n$ below 800 MeV. For that reason, we did not use TAPS in our analysis. The CB was installed in the tagged bremsstrahlung photon beam of the Mainz Microtron (MAMI) [25,26], with the photon energies determined by the Glasgow tagging spectrometer [27–29].

The CB spectrometer is a sphere consisting of 672 optically isolated NaI(Tl) crystals, shaped as truncated triangular pyramids, which point toward the center of the sphere. Each crystal is 41 cm long, which corresponds to 15.7 radiation lengths. The crystals are arranged in two hemispheres that cover 93% of 4π sr, sitting outside a central spherical

cavity with a radius of 25 cm, which is designed to hold the target and inner detectors. The CB calorimeter covers polar angles from $20°$ to $160°$ with full azimuthal coverage. The energy resolution for EM showers in the CB can be described as $\Delta E/E = 0.020/(E[\text{GeV}])^{0.36}$ [24]. Shower directions are determined with a resolution in θ, the polar angle with respect to the beam axis, of $\sigma_\theta = 2°$–$3°$, under the assumption that the photons are produced in the center of the CB. The resolution in the azimuthal angle ϕ is $\sigma_\theta/\sin\theta$. That is an intrinsic CB resolution, while in the experiment, the angular resolution in θ is mainly defined by the target length. The CB calorimeter is well suited for detection of both charged particles and γ quanta. Simultaneously, the CB can be used to detect neutrons in a wide range of energies [30,31].

The Mainz Microtron (MAMI) is a four-stage accelerator, and its latest addition (the fourth stage) is a harmonic double-sided electron accelerator [26]. In this experiment, only the first three accelerator stages were used to produce an 883 MeV electron beam. Bremsstrahlung photons, produced by electrons in a 10 μm Cu radiator and collimated by a 4-mm-diameter Pb collimator, were incident on a 10-cm-long, 4-cm-diameter liquid deuterium target (LD$_2$) located in the center of the CB. The energies of the incident photons were analyzed up to 813 MeV by detecting the postbremsstrahlung electrons in the Glasgow tagger [27–29].

The tagger is a broad-momentum-band, magnetic-dipole spectrometer that focuses postbremsstrahlung electrons onto a focal-plane detector, consisting of 352 half-overlapping plastic scintillators. The energy resolution of the tagged photons, which is about ± 1 MeV, is largely defined by the overlap region of two adjacent scintillation counters (a tagger channel) and the electron-beam energy used [29]. For a beam energy of 883 MeV, a tagger channel has a width of about 2 MeV for a photon energy 707 MeV [29]. Tagged photons are selected in the analysis by examining the correlation in time between a tagger channel and the experimental trigger derived from CB signals.

The LD$_2$ target is surrounded by a particle identification detector (PID) [32], which is a cylinder of length 50 cm and diameter 12 cm, built from 24 identical plastic scintillator segments, of thickness 0.4 cm. Outside the PID, there are two multiwire proportional chambers (MWPCs) which measure the three-dimensional coordinates of a charged track.

The experimental trigger had one main requirement—the sum of the pulse amplitudes from the CB crystals had to exceed a hardware threshold that corresponded to an energy deposit larger than 40 MeV. To select the reaction $\gamma n \to \pi^0 n$, we require that the final π^0 and neutron be detected by the CB. In this case, the number of clusters which fire, i.e., groups of adjacent crystals in which energy is deposited by a particle's interaction with the calorimeter, is equal to three.

To provide a check on the performance of the CB detector, and to evaluate the efficiency of the trigger, a comparison of the total measured cross section, after the empty-target background was subtracted, was made with the previously published total photoabsorption cross section measured by the DAPHNE experiment at MAMI [33,34]. This comparison is shown in Fig. 2 for photon energies from 180 to 820 MeV. In the $\Delta(1232)$ region, the new and previous data are in
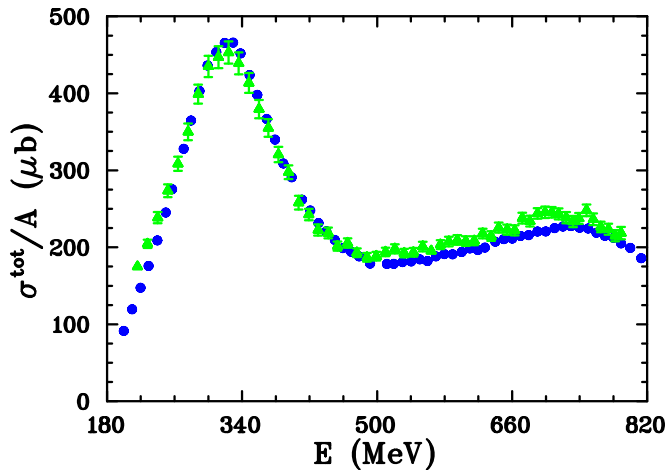
FIG. 2. The total photoabsorption cross section per nucleon as a function of incident photon energy. Filled blue circles (filled green triangles) are new A2 (previous DAPHNE [33,34]) measurements. Only statistical uncertainties are shown for all the data. The total normalization uncertainties of our data are about 3%.

agreement within the systematic uncertainties of the DAPHNE experiment (2.5%–3.0%) and the new measurements (~6%). Above 500 MeV, our cross-section data fall slightly below the previous measurements. The difference reaches 6% at 700 MeV. We do not apply any correction for the acceptance of the CB detector, but both the CB and DAPHNE detectors do have a similar inefficient region at forward angles. The correction for this inefficiency has been extensively studied in Ref. [32], where it is shown that the dominant contribution comes from single-charged-pion production, and the value of this correction is ~6%. Taking this into account, our data are in satisfactory agreement with the DAPHNE total photon absorption cross sections over the full photon energy range. This result demonstrates a high efficiency of the Crystal Ball detector for registering secondary particles and that the background present in the current measurement is small.

III. DATA HANDLING

The collected data allowed a detailed study of the reaction dynamics. The $\gamma n \to \pi^0 n$ differential cross sections were determined for 27 energy bins and the full range of production angles using model-dependent nuclear corrections to determine $\gamma n \to \pi^0 n$ data from measurements on the liquid deuterium target.

The main source of the background for our neutral channel is the reaction $\gamma p \to \pi^0 p$, where the high-energy proton was recorded by the PID detector, and such events were discarded from further analysis. Then the selection of the neutral pion is based on the search for two photons with an effective mass $m_{\gamma\gamma}$, close to the nominal mass of π^0 in the mass interval of 50 to 200 MeV. Reconstructed neutral pion and additional clusters in the CB calorimeter, to determine the direction of neutron emission, give complete reaction kinematics for $\gamma d \to \pi^0 np$.

Analysis of the shape of the proton momentum spectrum allows us to determine the background contribution arising from the production of two or more neutral pions. The distribution of the proton momentum spectrum is shown in Fig. 3, where the low-momentum component, corresponding to the Fermi momentum of nucleons in the deuteron [35], can be seen. It can be well described by the superposition of the Landau function [36] in the peak region and an exponential to the right of the peak. Thus, the background can be removed for the component located in the high-momentum region on the right side of the distribution. The background significantly increases with the initial photon energy and reaches up to ~40% at 800 MeV while it is almost zero at 200 MeV.

In this work, much attention was paid to the efficiency of neutron detection, knowledge of which is necessary to determine reaction cross sections. The thickness of CB crystals is one interaction length only, so it is impossible to measure neutron energy; however, it is possible to determine the location of the neutron interaction in the CB. This is enough for neutron detection efficiency measurements using the same data. It has been done in Ref. [37] by searching for the point of neutron interaction in the CB within a predicted direction from the kinematics of pion photoproduction on the deuteron with known kinematic parameters of a neutral pion and proton. It should be noted that the analysis of data at low photon energies is a rather difficult task. In this case, the neutron detection efficiency decreases with decreasing photon and neutron energies and is only a few percent at 20–30 MeV neutron energies, which can lead to inaccuracy in the analysis of experimental data. In addition to the CB calorimeter, the neutron detection threshold per cluster affects the efficiency of neutron detection. The ratio of the efficiency of neutron detection to simulation is shown in Fig. 4 (left) as a function of neutron momentum. To determine a full $\gamma n \to \pi^0 n$ reaction efficiency, the software package GEANT4 [38] was used in the simulation of the experiment. The event generator used a theoretical model based on a detailed description of the deuteron structure, taking into account the Fermi motion of nucleons in the deuteron and NN-FSI effects. To compare the results for the cross sections with the PWA predictions of SAID [13] and MAID [39], where the cross sections are given for the free neutron and neutron at rest [Fig. 4 (right)], it is necessary to take into account the corresponding corrections [40]. The calculations used corrections determined from the MAID2007 analysis. Corrections for the interaction effect in the final-state depending on the π^0 production angle in c.m. for different values of the incident photon energy are presented in Fig. 5. The effect of the FSI correction becomes significant, especially at low photon energies.

The photon flux is defined by counting the scattered electrons in the focal plane of the tagging system and correcting for the emitted photons lost in the collimator. The probability for bremsstrahlung photons to reach the target is measured periodically during data taking by a total-absorption lead glass counter, which is moved into the photon beam line at reduced photon intensity. Using this method, the tagging efficiency for an 883 MeV electron beam was determined to be approximately 35% with an accuracy of about 5%.
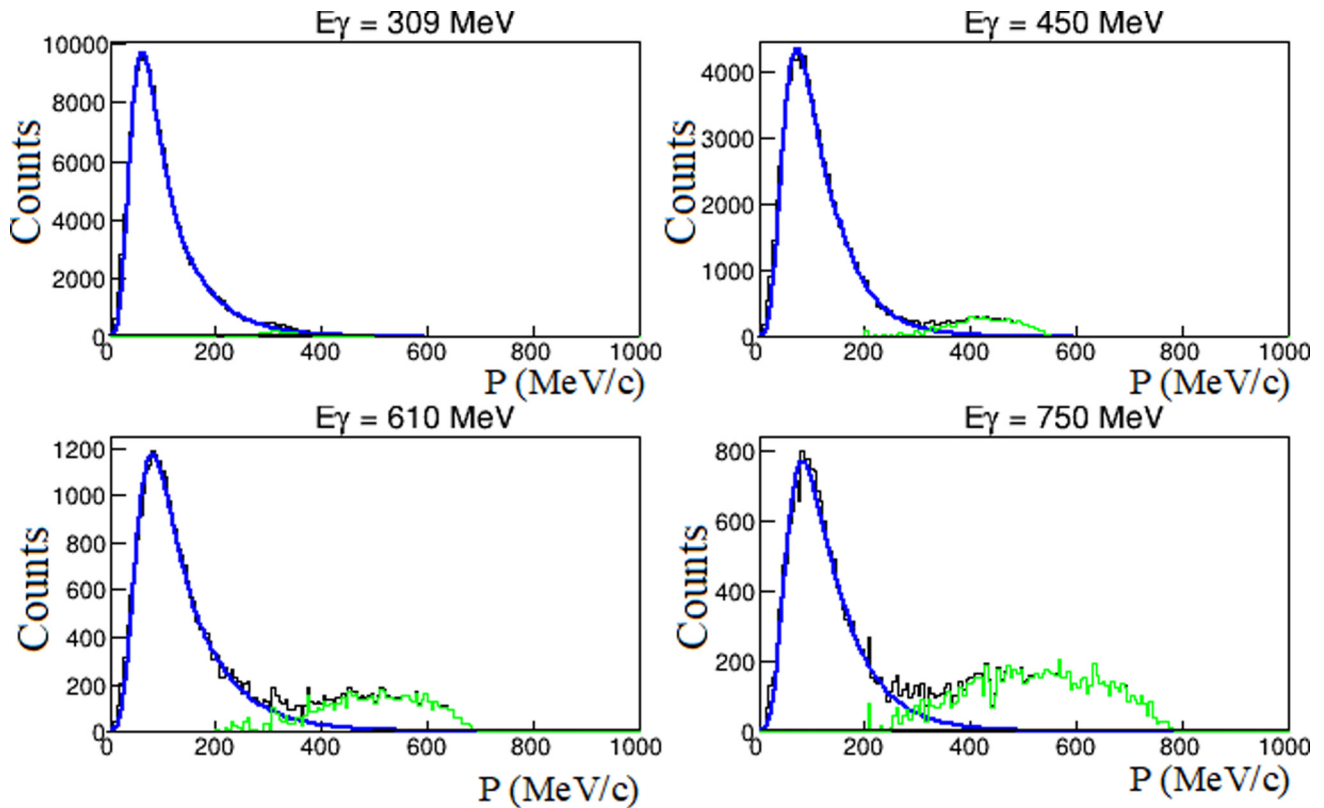
FIG. 3. Momentum distribution for low-energy protons for four initial photon energies. Experimental distributions (black) were fit by a Landau function in the peak region and an exponential to the right of the peak (blue). The background contribution is shown in green.

One of the main contributions to systematic uncertainties is the definition of the photon flux, which is based on the calculation of tagging efficiency. Another source of uncertainty is the background subtraction due to the empty target. This contribution is not large and has an order of 1%. The systematic uncertainty of the total photoabsorbtion cross section was defined by these two factors.

The analysis cuts and Monte Carlo simulations used to obtain the $\gamma n \to \pi^0 n$ total cross section introduced a further

uncertainty of the order of 1%–2%. Furthermore, the accuracy of the neutron detection efficiency leads to an additional uncertainty at low energies of ∼3%. So, the total overall uncertainty for the $\gamma n \to \pi^0 n$ total cross section is about 6%.

In the case of the $\gamma n \to \pi^0 n$ differential cross sections, the largest systematic uncertainties appear at forward and backward pion angles, where the statistical errors increase. This effect is actually due to the low efficiency of neutron detection. The typical systematic uncertainties at
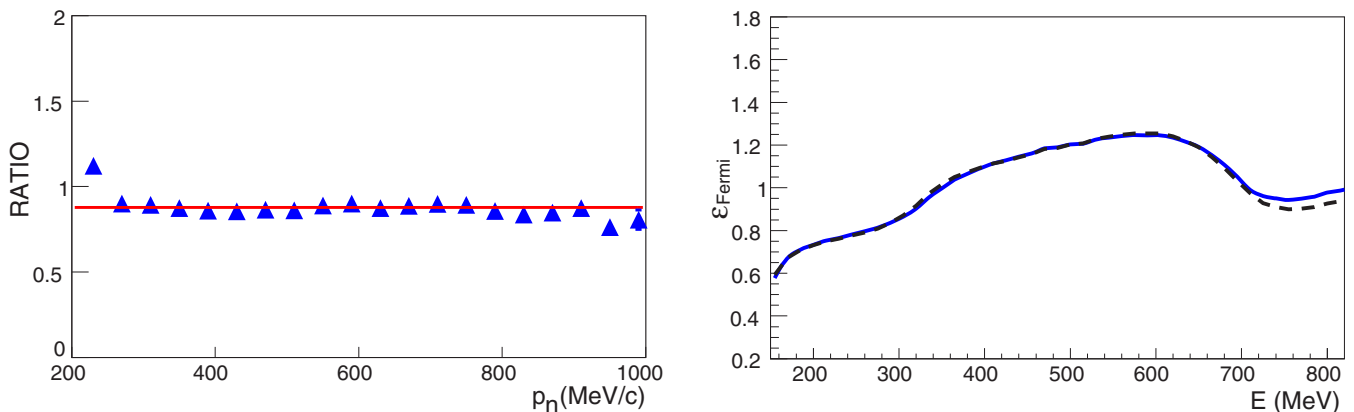

FIG. 4. Corrections for the reaction $\gamma n \to \pi^0 n$ cross sections. (left) Ratio of the efficiency of neutron detection to a simulation of the CB calorimeter vs neutron momentum. Solid red line corresponds to the average value of the ratio $= 0.878 \pm 0.004$. (right) The Fermi-momentum correction $\varepsilon_{\text{Fermi}}$ in the deuteron for recent SAID (blue solid line) and MAID (black dashed line) solutions vs initial photon energy.
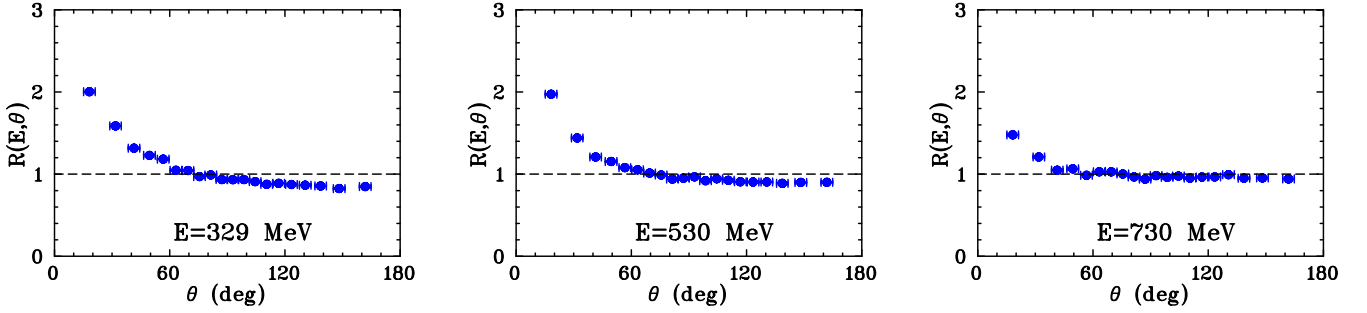
FIG. 5. The FSI correction factor $R(E, \theta)$ for selected beam energies vs the polar angle θ of the outgoing π^0 in the rest frame of the π^0 and the fast neutron. The normalization uncertainties are not shown.

these forward and backward pion angles are estimated to be $\sim 10\%$.

IV. FINAL-STATE INTERACTION

Exact determinations of the differential pion photoproduction cross sections on the neutron, based on experimental data for $\gamma d \to \pi^0 pn$, cannot be implemented without a reliable theoretical reaction model. This model was developed, taking into account the contribution not only of IA [Fig. 6 (left)], but also effects of NN and πN interactions in the final state. A detailed description of FSI effects is given in Refs. [10,11]. The SAID phenomenological amplitudes, from NN [41] and πN [6] elastic with $\gamma N \to \pi N$ [42] PWAs, were used as input for the GWU-ITEP code. The full Bonn potential [43] was used for the deuteron description, and Fermi motion of nucleons in the deuteron was taken into account. In this paper, to speed up numerical calculations, the model has been simplified. The contribution from πN-FSI, which is important close to the threshold, does not play a significant role above $E = 200$ MeV, as claimed in Ref. [44], and so was neglected here. The effect of NN-FSI was taken into account in the S-wave approximation which makes the dominant contribution. The parameters of the pn-scattering s-wave amplitudes with isospins 0 and 1 were taken from Ref. [45]. Thus, the amplitude M of the reaction $\gamma d \to \pi^0 pn$ (Fig. 6) is given as

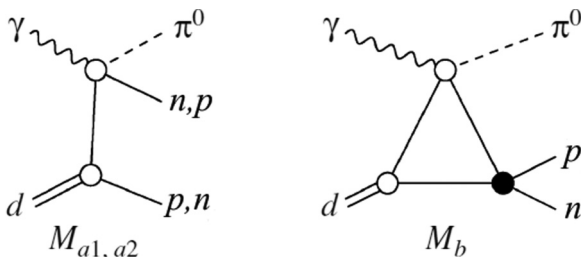$$M = M_{a1} + \Delta, \quad \Delta = M_{a2} + M_b, \quad (2)$$

FIG. 6. Feynman diagrams for the leading terms of the $\gamma d \to \pi^0 np$ amplitude: the impulse approximation (M_{a1}, M_{a2}) and NN-FSI (M_b). The wavy, dashed, solid, and double lines correspond to photons, pions, nucleons, and deuterons, respectively.

where M_{a1} is a leading IA diagram with the fast neutron and Δ is a correction that takes into account the pn-FSI (M_b) and IA diagram with regrouped nucleons (M_{a2}). The expressions for these amplitudes are given in detail in Appendix A of Ref. [11] [note that we did not include the off-shell factor for the $\gamma N \to \pi N$ amplitude, introduced in Ref. [11], Eq. (18)]. Calculating such a correction for the analysis of the experimental data means taking into account each event with a weight as

$$R = \frac{\overline{|M_{a1}|^2}}{\overline{|M|^2}}, \quad (3)$$

where $\overline{|M_{a1}|^2}$ and $\overline{|M|^2}$ are amplitude squares averaged over spins and calculated for the kinematics of the events. Furthermore, event handling was carried out under the assumption that the reaction mechanism is determined by the diagram M_{a1}.

We determine the differential cross sections of the reaction $\gamma n \to \pi^0 n$ from the measurements on the deuteron by using the theoretical model which describes the reaction $\gamma d \to \pi^0 pn$.

V. EXPERIMENTAL RESULTS

The differential cross section for the $\gamma n \to \pi^0 n$ reaction is defined by the formula:

$$\frac{d\sigma(E, \theta)}{d\Omega} = \sigma_0 \frac{\Delta N_{\text{Events}}}{N_{\text{Scaler}} \, \varepsilon_{\text{Tag}}}$$

$$\times \frac{1}{\varepsilon_{\text{Sel}} \, \varepsilon_{\text{Backg}} \, \varepsilon_{\text{PID}} \, \varepsilon_{\text{Fermi}} \, \varepsilon_{\text{FSI}} \, 2\pi \, d\cos(\theta)}, \quad (4)$$

where $\sigma_0 = \rho_{\text{targ}} L_{\text{targ}} N_A / 2 \times 10^{-7}$ (μb) is the nuclear density of the liquid deuterium target; ΔN_{Events} is the number of the events in $d\cos(\theta)$, where θ is the neutral pion production angle in c.m. relative to the beam axis; N_{Scaler} is the number of counts in the tagger scalers; ε_{Tag} is the tagging efficiency (fraction of photons impinging on the target); ε_{Sel} is the selection efficiency obtained from the simulated data, which also includes neutron detection efficiency incorporated into the Monte Carlo. The neutron detection efficiency is defined directly from data by the method proposed in Ref. [37]; $\varepsilon_{\text{Backg}}$ is the background extraction efficiency, which included
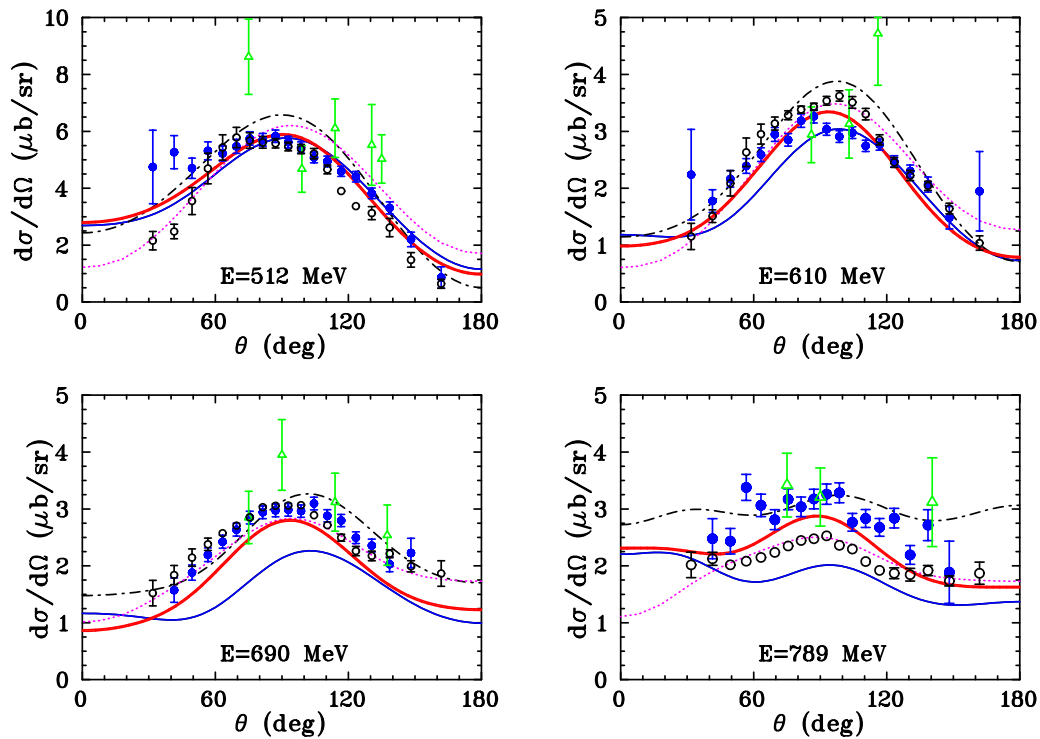
FIG. 7. Differential cross section for the reaction $\gamma n \to \pi^0 n$ vs π^0 c.m. polar angle for selected photon energies. Data: filled blue (open black) circles are new (previous [22]) A2 measurements, open green triangles are the previous non-MAMI measurements [5]. Only angle-dependent (statistical and systematical combined in quadratures) uncertainties are shown for all the data. The total normalization (angular independent) uncertainties of the cross section vary between 2% and 6.5% (not included in plots). Fits: SAID MA19 (red thick solid lines), recent SAID MA27 (blue solid lines) [13], MAID2007 (black dash-dotted lines) [39], and BnGa BG2014-02 (magenta dotted lines) [46].

the empty-target correction and the correction for random photons in the beam; $\varepsilon_{\rm PID}$ is the correction factor for the PID inefficiency, this value was estimated on the experimental data from CB and MWPC and required to select a neutral decay channel; $\varepsilon_{\rm FSI}$ is the FSI-effect correction to get the $\gamma n \to \pi^0 n$ cross section from the deuteron measurements, $\varepsilon_{\rm FSI} = R(E, \theta)^{-1}$ (see above).

Since our results for the $\gamma n \to \pi^0 n$ differential cross sections consist of 492 experimental points, they are not tabulated in this publication but are available in the SAID database [5] along with their uncertainties and the energy binning.

In Fig. 7, our differential cross sections for four incident photon energies are compared with previous measurements made at similar energies [5]. Some of these measurements [22] are quite recent while most of them were performed in the 1970s at Tokyo ($E = 396$–905 MeV) [47,48], Frascati ($E = 462$–784 MeV) [49], and SLAC ($E = 911$–1390 MeV) [50] bremsstrahlung facilities, demonstrating the general desire of the resonance-physics community to obtain new $\gamma N \to \pi N$ data, which are needed for a better determination of the properties of the N^* states. As seen in Fig. 7, all our results are in reasonable agreement with the previous measurements and significantly extend down to lower energies the previously published A2 data [22], covering the Δ-isobar resonance peak region. Some discrepancies are observed between the data obtained at forward production angles, but this can be explained by the rapidly falling cross section close

to the forward direction where the FSI correction increases (see Fig. 5).

Presented in Fig. 8 are total cross sections for $\gamma n \to \pi^0 n$, compared with PWA fits. There are two structures visible here, the first associated with the $\Delta(1232)3/2^+$, while a small structure is connected to $N(1520)3/2^-$ and $N(1535)1/2^-$.

The new SAID best fit results MA19 are in satisfactory agreement with the data at energies exceeding 300 MeV
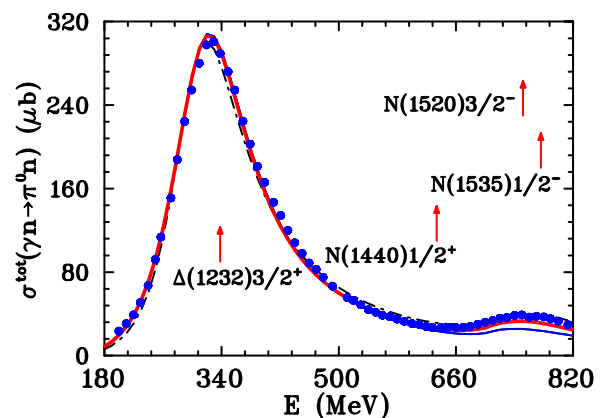

FIG. 8. Total cross section of the reaction $\gamma n \to \pi^0 n$ as a function of incident photon energy. Only statistical uncertainties are shown for the data. The total normalization uncertainties vary between 2% and 6.5%. Vertical red arrows show BW masses of low-lying resonances [1]. Notation is the same as in Fig. 7.
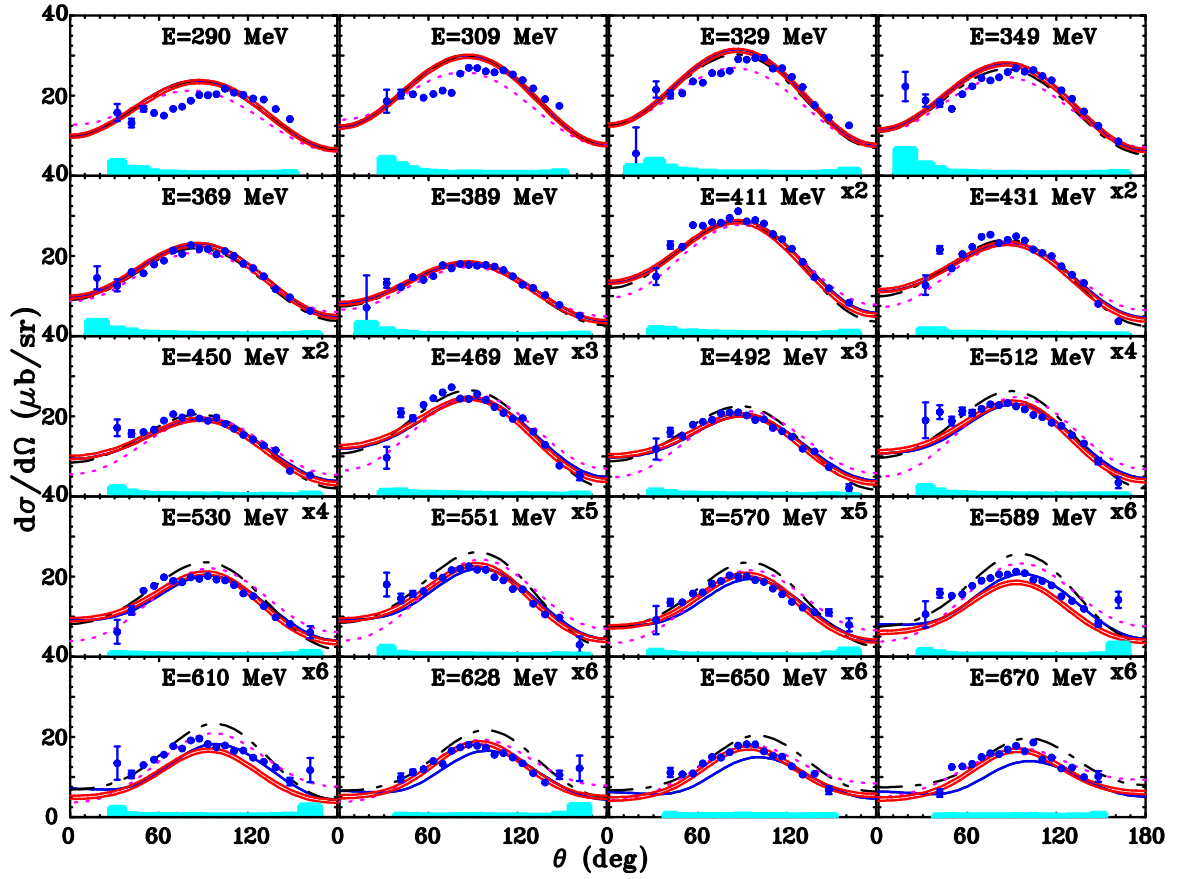
FIG. 9. Differential cross section for the reaction $\gamma n \to \pi^0 n$ below 680 MeV. Notation as in Fig. 7. Only statistical uncertainties are shown for all data. The angular-dependent systematic uncertainties are shown by cyan histograms.

(Figs. 9–11), and have visible discrepancies at lower energies (Fig. 9). Two reasons for this disagreement can be noted. First, this is due to the possible underestimation of the interaction effect in the final state, which becomes important in this particular energy range. The simplified FSI code, for example, does not take into account the contribution of the πN-FSI effects which, as a result, may lead to distortion of the shape of the spectra of differential cross sections. Second, the neutron detection efficiency varies with energy. It decreases with decreasing particle momentum and is only a few percent (see, for instance,

Fig. 9 of Ref. [37]), which can lead to large systematic errors.

VI. IMPACT OF THE PRESENT DATA ON PARTIAL-WAVE ANALYSIS

The SAID parametrization of the transition amplitude $T_{\alpha\beta}$ used in the hadronic fits to the πN scattering data is given as

$$T_{\alpha\beta} = \sum_{\sigma} \left[1 - \overline{K}C\right]^{-1}_{\alpha\sigma} \overline{K}_{\sigma\beta}, \tag{5}$$

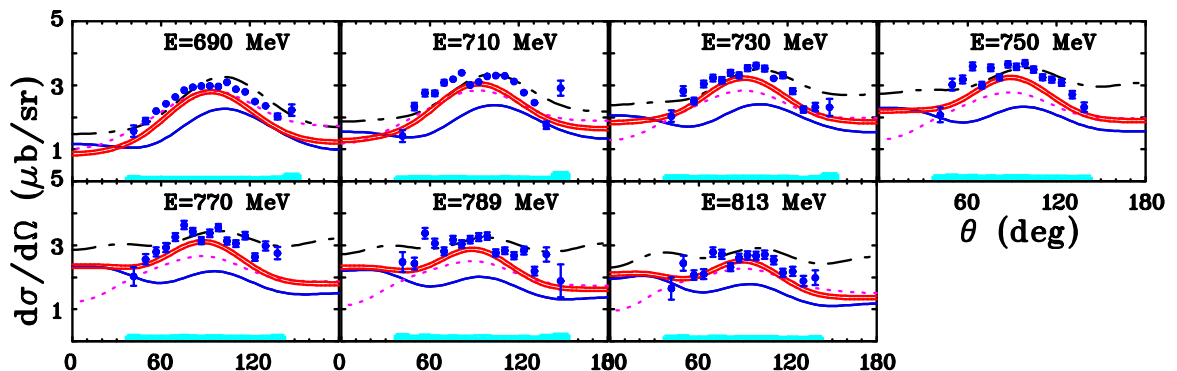FIG. 10. Differential cross section of the reaction $\gamma n \to \pi^0 n$ above 680 MeV. Notation is the same as in Fig. 9.
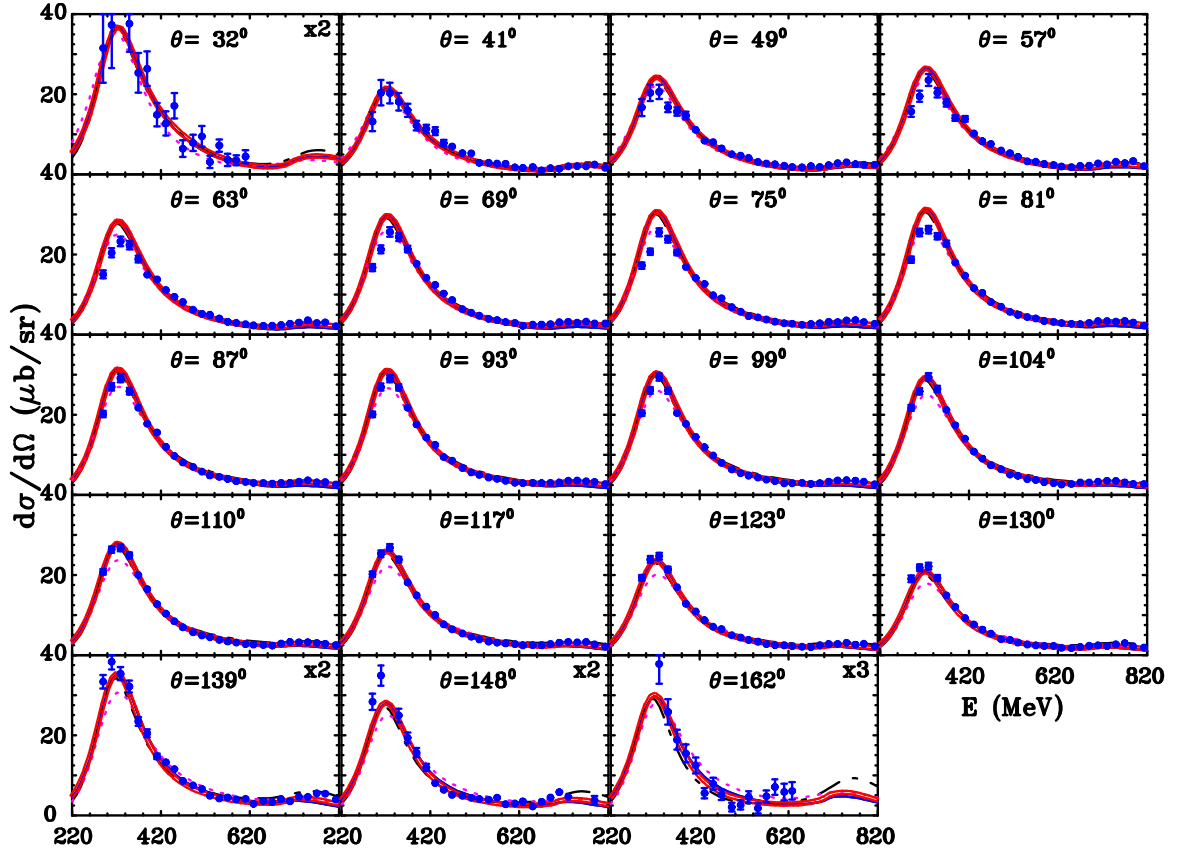
FIG. 11. Fixed-angle excitation function for the $\gamma n \rightarrow \pi^0 n$ reaction as a function of incident photon energy. The uncertainties shown are the angle-dependent statistical and systematic uncertainties, combined in quadrature. Notation is the same as in Fig. 9.

where α, β, and σ are channel indices for the πN, $\pi \Delta$, ρN, and ηN channels. Here $\overline{K}_{\alpha\beta}$ are the Chew-Mandelstam K matrices, which are parametrized as polynomials in the scattering energy. C_α is the Chew-Mandelstam function, an element of a diagonal matrix C in channel space, which is expressed as a dispersion integral with an imaginary part equal to the two-body phase space [51].

In Ref. [52], it was shown that this form could be extended to $T_{\alpha\gamma}$ to include the electromagnetic channel as

$$T_{\alpha\gamma} = \sum_\sigma \left[1 - \overline{K}C \right]^{-1}_{\alpha\sigma} \overline{K}_{\sigma\gamma}. \qquad (6)$$

Here, the Chew-Mandelstam K-matrix elements associated with the hadronic channels are kept fixed from the previous SAID solution SP06 [6], and only the EM elements are varied. The resonance pole and cut structures are also fixed from hadronic scattering. This provides a minimal description of the photoproduction process, where only the N^* and Δ^* states present in the SAID πN scattering amplitudes are included in this multipole analysis.

With each angular distribution, a normalization constant (X) and its uncertainty (ϵ_X) were assigned [53]. The quantity ϵ_X is generally associated with the systematic uncertainty (if known). The modified χ^2 function to be minimized is given by

$$\chi^2 = \sum_i \left(\frac{X\theta_i - \theta_i^{\text{expt}}}{\epsilon_i} \right)^2 + \left(\frac{X-1}{\epsilon_X} \right)^2, \qquad (7)$$

where the subscript i labels the data points within the distribution, θ_i^{expt} is an individual measurement, θ_i is the corresponding calculated value, and ϵ_i represents the total angle-dependent uncertainty. The total χ^2 is then found by summing over all measurements. This renormalization freedom often significantly reduces the overall χ^2 but may over-renormalize cross sections significantly beyond limits indicated by the systematic errors. This effect is evident when comparing the MA27 curve with the higher-energy data. By increasing the weight of the second term in our modified χ^2 function, this problem was avoided. The weight was increased until the fit renormalization factors remained inside limits suggested by the systematic errors. For other data analyzed in the fit, such as excitation data, the statistical and systematic uncertainties were combined in quadrature and no renormalization was allowed.

In the previous fits to the γn differential cross sections, the unrestricted best fit gave renormalization constants X significantly different from unity. As can be seen from Eq. (7), if an angular distribution contains many measurements with small statistical uncertainties, a change in the renormalization may improve the fit with only a modest χ^2 penalty. Here, however, the weight of the second term in Eq. (7) has been adjusted by the fit for each dataset to keep the renormalization constants approximately within ϵ_X of unity. This was possible without degrading the overall fit χ^2, as can be seen in Fig. 12. With the new high-precision $\gamma n \rightarrow \pi^0 n$ cross sections from
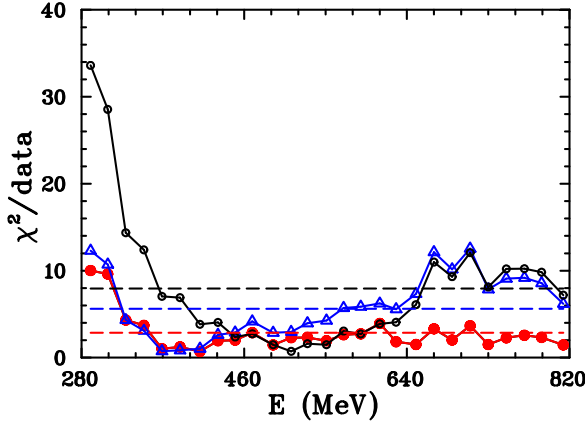
FIG. 12. Comparison of the previous SAID solution MA27 [13] applied to the present A2 data with (blue open triangles) and without (black open circles) FSI corrections and the new SAID MA19 (red full circles) solution obtained after adding the present A2 data with FSI corrections into the fit (the solid lines connecting the points are included only to guide the eye). Shown are the fit χ^2-per-data-point values averaged within each energy bin E, where the horizontal dashed lines [blue (black) for MA27 and red for MA19] show the overall χ^2-per-data-point values.

the present MAMI dataset, a new SAID multipole analysis has been completed. This new global energy-dependent (ED) solution has been labeled MA19. The overall fit quality of the present MA19 and previous SAID MA27 solutions are compared in Table II. The inclusion of the present dataset shows significant improvement in the comparisons between the SAID MA27 and MA19 solutions as shown in Fig. 12 and Table II. This demonstrates the power of these cross-section measurements with their small uncertainties. The overall comparison of the SAID MA19 and MA27 solutions in Table II shows that the fit χ^2-per-data values are essentially unchanged for pion photoproduction channels. The χ^2 per data = 3.77 for MAID2007 vs new present A2 measurements is understandable since many recent datasets were not included in this analysis.

Our next step is to extract the photon-decay amplitude at the pole. We do this by extracting all the pole positions and residues of the relevant partial waves and then we use the residues to obtain the final result, as described in Ref. [54].

Similarly as in Ref. [13], the Laurent + Pietarinen (L + P) method has been applied to determine the pole positions and residues from the pion photoproduction multipoles [55]. The driving concept behind the method is to replace the complexity of solving an elaborate theoretical model and analytically continuing its solution into the complex energy plane by using a local power-series representation of partial wave amplitudes that only exploits analyticity and unitarity. The L + P approach separates pole and regular parts in the form of a Laurent expansion and, instead of modeling the regular part by using some physical model, it uses the conformal-mapping-generated, rapidly converging power series with well-defined analytic properties called a Pietarinen expansion to represent it effectively. In other words, the method replaces the regular part, calculated in a model with the simplest analytic function that has the correct analytic properties of the analyzed partial wave (multipole), and which fits the given input. In such an approach, the model dependence is minimized and is reduced to the choice of the number and location of L + P branch points used in the model.

So, we expand the multipoles $M(W)$ in terms of a sum over all poles and with a Pietarinen series representing the energy-dependent regular (non-pole) part as

$$M(W) = \sum_{i=1}^{k} \frac{\alpha_{-1}^{(i)}}{W - W_i} + B^L(W). \tag{8}$$

Here W, $\alpha_{-1}^{(i)}$, and W_i are complex numbers representing the c.m. energy, residues, and pole positions for the ith pole, respectively, and $B^L(W)$ is a regular function in the whole complex plane. As shown in Ref. [56], a general unknown analytic function $B(W)$ with branch points in x_P, x_Q, and x_R can be expanded into a power series of Pietarinen functions as

$$B^L(W) = \sum_{n=0}^{M} c_n X(W)^n + \sum_{n=0}^{N} d_n Y(W)^n$$
$$+ \sum_{n=0}^{N} e_n Z(W)^n + \cdots,$$
$$X(W) = \frac{\alpha^2 - \sqrt{x_P - W}}{\alpha^2 + \sqrt{x_P - W}},$$

TABLE II. Average χ^2 per data [including information on the total χ^2 from Eq. (7) and the number of data points used] for MAID2007 [39] and two SAID solutions: MA27 [13] and MA19. To satisfy the MAID2007 energy limit, we are presenting results for data below $W = 2$ GeV or $E = 1650$ MeV. For the χ^2 per data of the MAID2007 solution, we took into account overall systematic errors as the SAID group does [53].

Reaction	MAID2007	SAID MA27	SAID MA19
Present			
$\gamma n \to \pi^0 n$	$1855/492 = 3.77$	$2765/492 = 5.62$	$1405/492 = 2.86$
Previous			
$\gamma p \to \pi^0 p$	$156\,700/13\,988 = 11.20$	$25\,856/13\,988 = 1.85$	$23\,954/13\,988 = 1.71$
$\gamma p \to \pi^+ n$	$121\,150/5225 = 23.19$	$10\,785/5225 = 2.06$	$10\,371/5225 = 1.99$
$\gamma n \to \pi^- p$	$49\,471/4142 = 11.94$	$7087/4142 = 1.71$	$6530/4142 = 1.58$
$\gamma n \to \pi^0 n$	$27\,060/515 = 52.54$	$2958/515 = 5.74$	$2320/515 = 4.51$
Total	$354\,373/23\,870 = 14.85$	$46\,686/23\,870 = 1.96$	$43\,174/23\,870 = 1.81$

TABLE III. Moduli [in $(\mathrm{GeV})^{-1/2} \times 10^{-3}$] and phases (in degrees) of the photon-decay amplitudes at the pole for neutron $A_{1/2}(n)$ and $A_{3/2}(n)$ from the SAID MA27 [13] and MA19 solutions. Pole results from the Bonn-Gatchina (BnGa) analysis are included for comparison [57] (BW values are from Ref. [58]). Kent State University (KSU) results are from Ref. [59]. BW values labeled with †.

Resonance	Coupling	SAID MA19	SAID MA27	BnGa	KSU
$N(1440)1/2^+$	$A_{1/2}(n)$	$80 \pm 10, 96° \pm 2°$	$65 \pm 5, 5° \pm 3°$	$43 \pm 12^{\dagger}$	$13 \pm 12^{\dagger}$
$N(1520)3/2^-$	$A_{3/2}(n)$	$-130 \pm 8, 20° \pm 6°$		$-113 \pm 2^{\dagger}$	$-123 \pm 6^{\dagger}$
$N(1520)1/2^-$	$A_{1/2}(n)$	$-47 \pm 4, 1° \pm 2°$		$-49 \pm 8^{\dagger}$	$-72 \pm 3^{\dagger}$
$N(1535)1/2^-$	$A_{1/2}(n)$	$-70 \pm 10, 2° \pm 5°$	$-55 \pm 5, 5° \pm 2°$	$-88 \pm 4, 5° \pm 4°$	$-55 \pm 6^{\dagger}$
$N(1650)1/2^-$	$A_{1/2}(n)$	$13 \pm 4, -50° \pm 15°$	$14 \pm 2, -30° \pm 10°$	$16 \pm 4, -28° \pm 10°$	$1 \pm 6^{\dagger}$

$$Y(W) = \frac{\beta^2 - \sqrt{x_Q - W}}{\beta^2 + \sqrt{x_Q - W}},$$

$$Z(W) = \frac{\gamma^2 - \sqrt{x_R - W}}{\gamma^2 + \sqrt{x_R - W}}, \qquad (9)$$

where c_n, d_n, e_n, and α, β, γ are real numbers that represent tuning parameters and coefficients of the Pietarinen functions $X(W)$, $Y(W)$, and $Z(W)$, respectively. A variable number of coefficients in three series of Eq. (9) were used, depending on the structure of the non-pole part of each amplitude.

When the input data statistically satisfy the normal distribution (meaning that they are acquired in a noncorrelated procedure), the estimation of the errors of all resulting pole parameters can be obtained directly from any standard minimization routine. However, in our case, the nearby energy points of the input multipoles are correlated through analyticity of the energy-dependent partial wave of the MA19 solution, so the standard error analysis cannot be used as the standardly defined χ^2 becomes extremely small ($\chi^2 \ll 1$) regardless of which error is attributed to the input. So, the error analysis of resulting parameters cannot be reliably performed.

In this paper, we improve this aspect of our model, and introduce a procedure that creates completely realistic errors for pole parameters extracted from ED MA19 partial waves. First, we have to attribute realistic errors to MA19 ED solutions. We do it by using MA19 single-energy (SE) analysis as the measure of how good an ED analysis actually is. We perform SE PWA at energies where we have an abundance of experimental data, and constrain it to an ED MA19 partial wave strong enough to achieve the continuity in energy, and weak enough to give enough freedom for the fit to move away as much as possible from the ED MA19 solution in coming maximally close to the experiment. In that way at each energy the SE solution maximally reproduces the available experimental data base, so we are definitely closer to experiment than the ED MA19 solution is. The probability that the true value lies inside the interval which is defined by the difference between partial wave values in the ED and SE points $\mathrm{dif} = PW_{ED}(W) - PW_{SE}(W)$ is, therefore, close to 100%, so we define the standard deviation of the partial wave ED value as $\sigma_{PW} = \mathrm{dif}/3$.

The next step is eliminating the correlations between neighboring energy points in the ED PW, which is introduced by the analyticity of the fitting function. This is done

by randomizing central values of the ED solution with PW standard deviation σ_{PW}, and assigning the error of the source ED error of the randomized point. In this way, we generate 1000 ensembles of randomized ED, which then independently fit, and an ensemble of 1000 pole parameters for the investigated partial waves was obtained. We confirm that the obtained ensemble corresponds to the normal distribution by generating the probability density function of the ensemble, and verifying that the shape of the obtained histogram is well reproduced with this, properly normalized, function. If this is the case, we then make a standard normal distribution error analysis of the generated ensemble, and pole parameters with realistic errors are obtained. In cases where this criterion is not matched, we have to modify the obtained ensemble by cutting out the points which erroneously enter this ensemble and which belong to the nearby local minimum of the L + P minimization procedure. When the new ensemble matches the criterion, we are free to make the desired error analysis. Once the pole position and residue were determined, the photon-decay amplitude at the pole could be constructed, as described in Ref. [54]. The residue of the corresponding πN elastic-scattering amplitude, required in this construction, was taken from the SAID analysis of elastic scattering data [6]. The spread of determinations found in Ref. [1] was used to estimate its uncertainty.

Final results for the photon-decay amplitudes are listed in Table III. Here comparisons are made with the Bonn-Gatchina (BnGa) and Kent State University (KSU) values and with an earlier SAID determination. For the $N(1520)$, the PDG2018 lists only BW values. This being the first determination of pole values, we compared at the level of moduli, finding good agreement. The agreement between BW and pole values is not as good for the Roper resonance, where the complicated pole-cut structure may invalidate this simple comparison of pole and BW quantities.

VII. SUMMARY AND CONCLUSION

The $\gamma n \to \pi^0 n$ differential cross sections have been measured at the tagged photon facility of the Mainz Microtron MAMI by using the Crystal Ball spectrometer. The data span the photon-energy range 290–813 MeV ($W = 1.195$–1.553 GeV) and from $18°$ to $162°$ c.m. angular range. The accumulation of 3.6×10^6 $\gamma n \to \pi^0 n$ events allows fine binning of the data in energy and angle, which will enable the

reaction dynamics to be studied in greater detail. The present differential cross-section data are in reasonable agreement with the previous measurements, but the energy binning is much finer and our measurements are in the very low energy range in the maximum of the Δ isobar. Our analysis includes FSI corrections. Additionally, the total photoabsorption cross section was measured.

Differential cross sections have visible discrepancies when compared with the predictions from SAID, MAID, and BnGa at energies below 300 MeV and are in satisfactory agreement with PWA results at higher energies.

A comparison of determinations for photon-decay amplitudes at the pole shows reasonably good agreement. The only noticeable exception is seen in the Roper photon-decay amplitude. Here, the difference may be due to the comparison of BW and pole-valued quantities. It will be interesting to see updated BnGa results at the pole once these data have been incorporated into new fits.

[1] M. Tanabashi *et al.* (Particle Data Group), Phys. Rev. D **98**, 030001 (2018).

[2] D. Drechsel and L. Tiator, J. Phys. G **18**, 449 (1992).

[3] K. M. Watson, Phys. Rev. **95**, 228 (1954).

[4] R. L. Walker, Phys. Rev. **182**, 1729 (1969).

[5] W. J. Briscoe, M. Döring, H. Haberzettl, I. I. Strakovsky, and R. L. Workman, Institute of Nuclear Studies of The George Washington University Database, http://gwdac.phys.gwu.edu/.

[6] R. A. Arndt, W. J. Briscoe, I. I. Strakovsky, and R. L. Workman, Phys. Rev. C **74**, 045205 (2006).

[7] R. L. Workman, R. A. Arndt, W. J. Briscoe, M. W. Paris, and I. I. Strakovsky, Phys. Rev. C **86**, 035202 (2012).

[8] A. B. Migdal, Sov. Phys. JETP **1**, 2 (1955) [JETP **28**, 10 (1955)].

[9] K. M. Watson, Phys. Rev. **88**, 1163 (1952).

[10] V. E. Tarasov, W. J. Briscoe, H. Gao, A. E. Kudryavtsev, and I. I. Strakovsky, Phys. Rev. C **84**, 035203 (2011).

[11] V. E. Tarasov, W. J. Briscoe, M. Dieterle, B. Krusche, A. E. Kudryavtsev, M. Ostrick, and I. I. Strakovsky, Phys. At. Nucl. **79**, 216 (2016).

[12] W. Chen *et al.*, Phys. Rev. C **86**, 015206 (2012).

[13] P. T. Mattione *et al.* (CLAS Collaboration), Phys. Rev. C **96**, 035204 (2017).

[14] W. J. Briscoe, A. E. Kudryavtsev, P. Pedroni, I. I. Strakovsky, V. E. Tarasov, and R. L. Workman, Phys. Rev. C **86**, 065207 (2012).

[15] S. Gardner *et al.* (A2 Collaboration at MAMI), Eur. Phys. J. A **52**, 333 (2016).

[16] J. R. M. Annand *et al.* (A2 Collaboration at MAMI), Phys. Rev. C **93**, 055209 (2016).

[17] S. Schumann *et al.* (A2 Collaboration at MAMI), Phys. Lett. B **750**, 252 (2015).

[18] P. Adlarson *et al.* (A2 Collaboration at MAMI), Phys. Rev. C **92**, 024617 (2015).

[19] M. H. Sikora *et al.* (A2 Collaboration at MAMI), Phys. Rev. Lett. **112**, 022501 (2014).

[20] D. Hornidge *et al.* (A2 and CB-TAPS Collaborations), Phys. Rev. Lett. **111**, 062004 (2013).

[21] M. Dieterle *et al.* (A2 Collaboration at MAMI), Phys. Lett. B **770**, 523 (2017).

[22] M. Dieterle *et al.* (A2 Collaboration at MAMI), Phys. Rev. C **97**, 065205 (2018).

[23] M. Dieterle *et al.* (A2 Collaboration at MAMI), Phys. Rev. Lett. **112**, 142001 (2014).

[24] A. Starostin *et al.* (Crystal Ball Collaboration), Phys. Rev. C **64**, 055205 (2001).

[25] H. Herminghaus *et al.*, IEEE Trans. Nucl. Sci. **30**, 3274 (1983).

[26] K. H. Kaiser *et al.*, Nucl. Instrum. Methods Phys. Res., Sect. A **593**, 159 (2008).

[27] I. Anthony, J. D. Kellie, S. J. Hall, G. J. Miller, and J. Ahrens, Nucl. Instrum. Methods Phys. Res., Sect. A **301**, 230 (1991).

[28] S. J. Hall, G. J. Miller, R. Beck, and P. Jennewein, Nucl. Instrum. Methods Phys. Res., Sect. A **368**, 698 (1996).

[29] J. C. McGeorge *et al.*, Eur. Phys. J. A **37**, 129 (2008).

[30] T. D. S. Stanislaus *et al.*, Nucl. Instrum. Methods Phys. Res., Sect. A **462**, 463 (2001).

[31] S. A. Bulychjov, A. E. Kudryavtsev, V. V. Kulikov, M. A. Martemianov, V. E. Tarasov, M. A. Lizunova, W. J. Briscoe, and I. I. Strakovsky, KnE Energ. Phys. **3**, 51 (2018).

[32] D. P. Watts (for Crystal Ball@MAMI Collaboration), *Proceedings of the 11th International Conference on Calorimetry in Particle Physics*, Perugia, Italy, 2004 (World Scientific, Singapore, 2005), p. 560.

[33] M. MacCormick *et al.*, Phys. Rev. C **53**, 41 (1996).

[34] M. MacCormick *et al.*, Phys. Rev. C **55**, 1033 (1997).

[35] R. L. Cool, G. Giacomelli, T. F. Kycia, B. A. Leontic, K. K. Li, A. Lundby, J. Teiger, and C. Wilkin, Phys. Rev. D **1**, 1887 (1970).

[36] L. Landau, J. Phys. (USSR) **8**, 201 (1944).

[37] M. Martemianov *et al.* (A2 Collaboration at MAMI), JINST **10**, T04001 (2015).

[38] J. Allison *et al.*, Nucl. Instrum. Methods Phys. Res., Sect. A **835**, 186 (2016).

[39] D. Drechsel, S. S. Kamalov, and L. Tiator, Eur. Phys. J. A **34**, 69 (2007); the MAID analyses are available through the Mainz website, http://maid.kph.uni-mainz.de/.

[40] S. A. Bulychev, A. E. Kudryavtsev, V. V. Kulikov, M. A. Martem'yanov, V. E. Tarasov, W. J. Briscoe, and I. I. Strakovsky, Phys. Atom. Nucl. **80**, 1549 (2017); [Yad. Fiz. **7**, 374 (2016)].

[41] R. A. Arndt, W. J. Briscoe, I. I. Strakovsky, and R. L. Workman, Phys. Rev. C **76**, 025209 (2007).

[42] M. Dugger *et al.* (CLAS Collaboration), Phys. Rev. C **76**, 025211 (2007).

[43] R. Machleidt, Phys. Rev. C **63**, 024001 (2001).

[44] M. I. Levchuk, A. Y. Loginov, A. A. Sidorov, V. N. Stibunov, and M. Schumacher, Phys. Rev. C **74**, 014004 (2006).

[45] L. D. Landau and E. M. Lifshits, *Quantum Mechanics: Non-Relativistic Theory* (Pergamon Press, London, 1958).

[46] D. Werthmüller *et al.*, Phys. Rev. C **90**, 015205 (2014); the Bonn-Gatchina analyses are available through the Bonn website, http://pwa.hiskp.uni-bonn.de/.

[47] Y. Hemmi *et al.*, Nucl. Phys. B **55**, 333 (1973).

[48] A. Ando, in *Physik-Daten, Physics Data*, Sekt. 7 *Compilation of Pion Photoproduction Data*, edited by H. Behrens, G. Ebel, D. Menze, W. Pfeil, and R. Wilcke (Physikalisches Institut der Universitaet, Bonn, Germany, 1977), Vol. 1.

[49] C. Bacci *et al.*, Phys. Lett. B **39**, 559 (1972).

[50] C. R. Clinesmith, Ph.D. thesis, California Institute of Technology, 1967.

[51] R. A. Arndt, J. M. Ford, and L. D. Roper, Phys. Rev. D **32**, 1085 (1985).

[52] R. L. Workman, M. W. Paris, W. J. Briscoe, and I. I. Strakovsky, Phys. Rev. C **86**, 015202 (2012).

[53] R. A. Arndt, W. J. Briscoe, I. I. Strakovsky, and R. L. Workman, Phys. Rev. C **66**, 055213 (2002).

[54] R. L. Workman, L. Tiator, and A. Sarantsev, Phys. Rev. C **87**, 068201 (2013).

[55] A. Švarc, M. Hadžimehmedović, H. Osmanović, J. Stahov, L. Tiator, and R. L. Workman, Phys. Rev. C **89**, 065208 (2014).

[56] A. Švarc, M. Hadžimehmedović, H. Osmanović, J. Stahov, L. Tiator, and R. L. Workman, Phys. Rev. C **88**, 035206 (2013).

[57] A. V. Anisovich, V. Burkert, E. Klempt, V. A. Nikonov, A. V. Sarantsev, and U. Thoma, Phys. Rev. C **95**, 035211 (2017).

[58] A. V. Anisovich, V. Burkert, E. Klempt, V. A. Nikonov, A. V. Sarantsev, and U. Thoma, Eur. Phys. J. A **49**, 67 (2013).

[59] B. C. Hunt and D. M. Manley, Phys. Rev. C **99**, 055205 (2019).